Communication

Scattering Analysis of Modulated Corrugations in a Conducting Circular Cylinder and Study of RCS Reduction

Sangsu Lee, Kyung-Young Jung[ID], Hosung Choo[ID], and Yong Bae Park[ID]

Abstract—In this communication, an electromagnetic boundary-value problem of modulated transverse corrugations in an infinite conducting circular cylinder is rigorously solved based on the Fourier transform, eigenfunction expansion, and the mode matching method. Radar cross section (RCS) of the modulated transverse corrugations is represented in the series form. Computation is performed to analyze scattering characteristics while varying depth, width, and period of the corrugations and to investigate the excitation of surface waves and concomitant RCS reduction.

Index Terms—Mode matching method, radar cross section (RCS), surface waves, transverse corrugations.

I. INTRODUCTION

A corrugated surface has been extensively investigated due to its wide applications in horn antennas, waveguide filters, and extraordinary optical transmission [1]–[4]. It is also known that the corrugated surface can be used to realize artificial soft or hard surfaces [5], [6]. The enhanced optical transmission through slits surrounded by periodic corrugations on the surface results from the surface plasmon polariton (SPP) resonance [7]. In fact, SPP modes are the special transverse magnetic surface wave modes propagating along the interface between two media that have positive and negative permittivities in the optical region. The SPP modes are evanescently decaying in the perpendicular direction to the interface because they are tightly bounded in the horizontal direction. Meanwhile, spoof SPP modes can be sustained by a perfect electric conductor (PEC) even in the micro/millimeter wave regimes when its surface is periodically corrugated [8]–[10]. Since they are bound electromagnetic surface waves that mimic the SPP modes in the optical region from the perspective of dispersion relation, the spoof SPP modes are also referred to as SPP-like modes or designer SPPs [9], [10]. Some previous studies have shown that the spoof SPP modes can be generated along

S. Lee and Y. B. Park are with the Department of Electrical and Computer Engineering, Ajou University, Suwon 16499, South Korea (e-mail: lss1507@ajou.ac.kr; yong@ajou.ac.kr).

K.-Y. Jung is with the Department of Electronic Engineering, Hanyang University, Seoul 04763, South Korea (e-mail: kyjung3@hanyang.ac.kr).

H. Choo is with the School of Electronic and Electrical Engineering, Hongik University, Seoul 04066, South Korea (e-mail: hschoo@hongik.ac.kr).

the surface of the conducting circular cylinder with periodic transverse corrugations [11]–[14]. The spoof SPP modes sustained over the surface of the transversely corrugated conducting cylinder have been mainly investigated for focusing and energy concentration. Analyses of the transverse corrugations in the circular cylinder have also been conducted for electromagnetic scattering in terms of the artificial hard surface or the geometry of the corrugation [15]–[18]. However, the previous studies assumed that the number of corrugations is infinite, and therefore, Floquet's theorem was used to represent the electromagnetic field. Moreover, the corrugations are assumed to be filled with dielectric material to satisfy the hard surface boundary condition. Thus, research on electromagnetic scattering from the circular cylinder with finite transverse corrugations may seem to be lacking. Finite corrugations or slots in a hollow circular cylinder can be rigorously analyzed based on the mode matching method, the Fourier transform, and eigenfunction expansion [19], [20]. Therefore, it is of great interest to rigorously solve the boundary-value problem for a nonperiodic corrugation using the mode matching method and to analyze electromagnetic scattering from the transversely corrugated conducting circular cylinder in the viewpoint of the spoof SPP modes. A previous study showed that the spoof SPP modes can be generated at multiple frequencies by modulating the geometry of rectangular grooves in a planar conductor based on in-depth simulations [21]. Thus, it is significantly meaningful to investigate the excitation of the spoof SPP modes and the feasibility of reducing the reflection at multiple spoof SPP resonance frequencies by modifying the geometry of the corrugations.

In this communication, an electromagnetic boundary-value problem of the modulated transverse corrugations in an infinite conducting circular cylinder is rigorously solved based on the mode matching method. The Fourier transform and eigenfunction expansion are used to represent the electromagnetic field in each region with respect to discrete and continuous modes. The boundary conditions are enforced to obtain a set of simultaneous equations for modal coefficients. Radar cross section (RCS) is represented in the series form. Computation is performed to analyze the excitation of surface waves and scattering characteristics in terms of the corrugation geometries in detail. To validate our formulation, the simulation results of Microwave Studio (MWS) of CST are compared to ours. In addition, a relationship between the excitation of the spoof SPP modes and the reduction of reflection is discussed.

II. FIELD ANALYSIS

Let us assume that a linearly TM-polarized uniform plane wave impinges on a conducting circular cylinder with narrow transverse corrugations at $\phi = 180°$ and $\theta = 90°$ (normal incidence), as shown in Fig. 1. A time convention $e^{j\omega t}$ is suppressed throughout the analysis. The permittivity and permeability in regions (I) and (II) are ϵ_1, μ_1, $\epsilon_2^{(i)}$, $\mu_2^{(i)}$. Superscript (i) indicates the ith corrugation from the bottom ($-z$-axis). In region (I) ($\rho > b$), the total electromagnetic
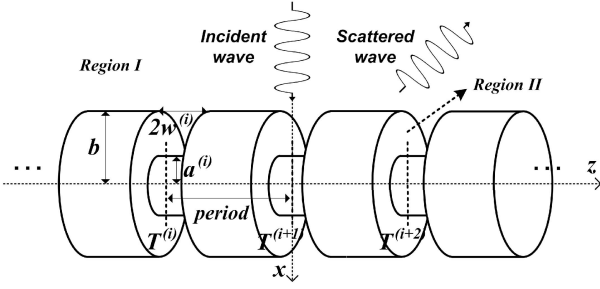
Fig. 1. Problem geometry.

field consists of incident, reflected, and scattered fields. In the cylindrical coordinates, the incident and reflected waves have the form of [22]

$$\vec{E}_t^i(\rho, \phi, z) = \hat{z} \sum_{n=-\infty}^{\infty} j^{-n} J_n(k_1 \rho) e^{jn\phi} \tag{1}$$

$$\vec{H}_t^i(\rho, \phi, z) = \hat{\phi} \frac{k_1}{j\omega\mu_1} \sum_{n=-\infty}^{\infty} j^{-n} J_n'(k_1 \rho) e^{jn\phi} \tag{2}$$

$$\vec{E}_t^r(\rho, \phi, z) = -\hat{z} \sum_{n=-\infty}^{\infty} j^{-n} \frac{J_n(k_1 b)}{H_n^{(2)}(k_1 b)} H_n^{(2)}(k_1 \rho) e^{jn\phi} \tag{3}$$

$$\vec{H}_t^r(\rho, \phi, z) = -\hat{\phi} \frac{k_1}{j\omega\mu_1} \sum_{n=-\infty}^{\infty} j^{-n} \frac{J_n(k_1 b)}{H_n^{(2)}(k_1 b)} H_n^{(2)\prime}(k_1 \rho) e^{jn\phi} \tag{4}$$

where $k_1 = \omega\sqrt{\mu_1\epsilon_1}$, $J_n(\cdot)$ is the Bessel function of the first kind of order n, $H_n^{(2)}(\cdot)$ is the Hankel function of the second kind of order n, and the prime denotes partial derivative with respect to the entire argument of both the Bessel and Hankel functions. The scattered field generated by the corrugations in the circular cylinder can be represented using the magnetic and electric vector potentials based on the Fourier transform [23]

$$A_z^I(\rho, \phi, z) = \sum_{n=-\infty}^{\infty} e^{jn\phi} \frac{1}{2\pi} \int_{-\infty}^{\infty} \tilde{A}_z^I(\zeta) H_n^{(2)}(\kappa_1 \rho) e^{j\zeta z} d\zeta \tag{5}$$

$$F_z^I(\rho, \phi, z) = \sum_{n=-\infty}^{\infty} e^{jn\phi} \frac{1}{2\pi} \int_{-\infty}^{\infty} \tilde{F}_z^I(\zeta) H_n^{(2)}(\kappa_1 \rho) e^{j\zeta z} d\zeta \tag{6}$$

where $\kappa_1 = \sqrt{k_1^2 - \zeta^2}$. In region (II) $(a^{(i)} < \rho < b, T^{(i)} - w^{(i)} < z < T^{(i)} + w^{(i)})$, the corrugations are assumed to be narrow for ease in computation because of the subwavelength condition for sustaining surface waves in general. Thus, the electromagnetic field within the corrugations can be considered to be uniform in the z-direction; the electromagnetic field does not vary with variable z [20]. This assumption is valid if the corrugations are sufficiently small compared to wavelength. In order to simplify the mode matching analysis procedure, we apply the inner boundary condition $(\rho = a^{(i)})$ when defining vector potentials. The tangential electric fields, E_ϕ and E_z, should be equal to 0 at $\rho = a^{(i)}$, and then the magnetic and electric vector potentials can be represented as a function of ρ and ϕ as follows:

$$A_z^{II}(\rho, \phi, z) = \sum_{i=1}^{L} \sum_{n=-\infty}^{\infty} C_n^{(i)} [J_n(k_2^{(i)} \rho) Y_n(k_2^{(i)} a^{(i)})$$
$$- J_n(k_2^{(i)} a^{(i)}) Y_n(k_2^{(i)} \rho)] e^{jn\phi} \tag{7}$$

$$F_z^{II}(\rho, \phi, z) = \sum_{i=1}^{L} \sum_{n=-\infty}^{\infty} D_n^{(i)} [J_n(k_2^{(i)} \rho) Y_n'(k_2^{(i)} a^{(i)})$$
$$- J_n'(k_2^{(i)} a^{(i)}) Y_n(k_2^{(i)} \rho)] e^{jn\phi} \tag{8}$$

where $k_2^{(i)} = \omega\sqrt{\mu_2^{(i)}\epsilon_2^{(i)}}$, $C_n^{(i)}$ and $D_n^{(i)}$ are the discrete modal coefficients of the ith corrugation, and $Y_n(\cdot)$ is the Bessel function of the second kind of order n. After the electromagnetic fields in all regions are defined, the boundary conditions are enforced to obtain a set of simultaneous equations for the modal coefficients at $\rho = b$. First, applying the Fourier transform $\int_{-\infty}^{\infty}(\cdot)e^{-j\zeta z} dz$ to E_z and E_ϕ continuities yields

$$\tilde{A}_z^I(\zeta) = \sum_{i=1}^{L} C_n^{(i)} \frac{k_1^2}{\kappa_1^2} I_1^{in} \frac{1}{H_n^{(2)}(\kappa_1 b)} P^{(i)}(\zeta) \tag{9}$$

$$\tilde{F}_z^I(\zeta) = \sum_{i=1}^{L} C_n^{(i)} \left(-j\frac{\omega\epsilon_1 n\zeta}{b\kappa_1^3}\right) I_1^{(i)} \frac{1}{H_n^{(2)\prime}(\kappa_1 b)} P^{(i)}(\zeta)$$
$$+ \sum_{i=1}^{L} D_n^{(i)} \frac{\epsilon_1 k_2^{(i)}}{\epsilon_2^{(i)}\kappa_1} I_2^{in} \frac{1}{H_n^{(2)\prime}(\kappa_1 b)} P^{(i)}(\zeta) \tag{10}$$

where

$$I_1^{in} = J_n(k_2^{(i)} b) Y_n(k_2^{(i)} a^{(i)}) - J_n(k_2^{(i)} a^{(i)}) Y_n(k_2^{(i)} b) \tag{11}$$

$$I_2^{in} = J_n'(k_2^{(i)} b) Y_n'(k_2^{(i)} a^{(i)}) - J_n'(k_2^{(i)} a^{(i)}) Y_n'(k_2^{(i)} b) \tag{12}$$

$$P^{(i)}(\zeta) = \frac{j}{\zeta} [e^{-j\zeta w^{(i)}} - e^{j\zeta w^{(i)}}] e^{-j\zeta T^{(i)}}. \tag{13}$$

Afterward, applying the orthogonality $\int_{T^{(l)}-w^{(l)}}^{T^{(l)}+w^{(l)}}(\cdot) dz$ to H_z and H_ϕ continuities yields

$$\sum_{i=1}^{L} C_n^{(i)} \left(-\frac{n}{\mu_1 b}\right) I_1^{in} J_1 + \sum_{i=1}^{L} D_n^{(i)}$$
$$\times \left[\left(-j\frac{k_2^{(i)}}{\omega\mu_1\epsilon_2^{(i)}}\right) I_2^{in} J_2 + j2\omega I_3^{ln} w^{(l)} \delta_{il}\right] = 0 \tag{14}$$

$$\sum_{i=1}^{L} C_n^{(i)} \left[\left(\frac{n^2}{\mu_1 b^2}\right) I_1^{in} J_3 - \frac{k_1^2}{\mu_1} I_1^{in} J_4 + \frac{2k_2^{(l)}}{\mu_2^{(l)}} I_4^{ln} w^{(l)} \delta_{il}\right]$$
$$+ \sum_{i=1}^{L} D_n^{(i)} \left(j\frac{nk_2^{(i)}}{\omega\mu_1\epsilon_2^{(i)} b}\right) I_2^{in} J_1 = -\frac{2k_1}{j\omega\mu_1} j^{-n}$$
$$\times \left[J_n'(k_1 b) - \frac{J_n(k_1 b)}{H_n^{(2)}(k_1 b)} H_n^{(2)\prime}(k_1 b)\right] w^{(l)} \tag{15}$$

where δ_{il} is the Kronecker delta function and

$$I_3^{ln} = J_n(k_2^{(l)} b) Y_n'(k_2^{(l)} a^{(l)}) - J_n'(k_2^{(l)} a^{(l)}) Y_n(k_2^{(l)} b) \tag{16}$$

$$I_4^{ln} = J_n'(k_2^{(l)} b) Y_n(k_2^{(l)} a^{(l)}) - J_n(k_2^{(l)} a^{(l)}) Y_n'(k_2^{(l)} b) \tag{17}$$

$$J_1 = \frac{1}{2\pi} \int_{-\infty}^{\infty} \frac{\zeta}{\kappa_1} \frac{H_n^{(2)}(\kappa_1 b)}{H_n^{(2)\prime}(\kappa_1 b)} P^{(i)}(\zeta) P^{(l)}(-\zeta) d\zeta \tag{18}$$

$$J_2 = \frac{1}{2\pi} \int_{-\infty}^{\infty} \kappa_1 \frac{H_n^{(2)}(\kappa_1 b)}{H_n^{(2)\prime}(\kappa_1 b)} P^{(i)}(\zeta) P^{(l)}(-\zeta) d\zeta \tag{19}$$

$$J_3 = \frac{1}{2\pi} \int_{-\infty}^{\infty} \frac{\zeta^2}{\kappa_1^3} \frac{H_n^{(2)}(\kappa_1 b)}{H_n^{(2)\prime}(\kappa_1 b)} P^{(i)}(\zeta) P^{(l)}(-\zeta) d\zeta \tag{20}$$

$$J_4 = \frac{1}{2\pi} \int_{-\infty}^{\infty} \frac{1}{\kappa_1} \frac{H_n^{(2)\prime}(\kappa_1 b)}{H_n^{(2)}(\kappa_1 b)} P^{(i)}(\zeta) P^{(l)}(-\zeta) d\zeta. \tag{21}$$

To calculate the integral form, we use the Gaussian quadrature integration. With the set of the simultaneous equations (14) and (15), the discrete modal coefficients $C_n^{(i)}$ and $D_n^{(i)}$ can be calculated.

III. RCS Calculation

Three-dimensional RCS is defined as [22]

$$\sigma_{3\text{-}D} = \lim_{r \to \infty} 4\pi r^2 \frac{\left| E_z^r + E_z^s \right|^2}{\left| E_z^i \right|^2}. \qquad (22)$$

We need to calculate the reflected field and the scattered field for the evaluation of RCS. The reflected field is the scattered field produced by the smooth circular cylinder in our formulation, and therefore, the reflected field in the far-field region can be calculated by using the equivalent surface current density. Therefore, the reflected field in the far-field region, E_z^r, can have the following form of [22]:

$$E_z^r = -\sin\theta \frac{jk_1 e^{-jk_1 r}}{4\pi r} \eta_1 \iint_S J_z \sin\theta e^{jk_1 r' \cos\psi} ds' \qquad (23)$$

where $\eta_1 = \sqrt{\mu_1/\epsilon_1}$ is the wave impedance. In general, calculating the integral form in (5) and (6) for the scattered field is not easy and also time-consuming. In addition, for the far-field radiation from slots on the circular cylinder, the surface equivalence theorem is not able to give an exact solution due to the curvature of the circular cylinder [22]. However, fortunately, the integral form could be removed when dealing with the scattered field in the far-field region. Specifically, in the far-field region, the circular cylinder can be assumed to be an infinitesimal dipole source. Then, the far-field electromagnetic field derived using different approaches in the Fourier domain and the frequency domain should be equal, given the uniqueness principle. Therefore, the integral form in (5) and (6) can be removed, as described in [23]. Then, the scattered field, E_z^s, produced by the transverse corrugations can have the form of

$$E_z^s = -j\omega(\sin\theta)^2 \frac{e^{-jk_1 r}}{\pi r} \sum_{n=-\infty}^{\infty} j^{n+1} \tilde{A}_z^I (-k_1 \cos\theta) e^{jn\phi}. \qquad (24)$$

The numerator in (22) becomes equivalent to the sum of the above reflected (23) and scattered (24) fields.

IV. Numerical Results

In order to investigate scattering characteristics of an infinite conducting circular cylinder with transverse corrugations in detail, we designed two models of the structure to excite surface waves at a different frequency, i.e., an array of smaller corrugations with a short period and that of larger corrugations with a long period. The former has a period 20 mm, $T^{(1)} = -60$ mm, $a^{(i)} = 26$ mm, $b = 30$ mm, $2w^{(i)} = 1.4$ mm, and $L = 7$. We will call it the first type. The latter has a period 30 mm, $T^{(1)} = -75$ mm, $a^{(i)} = 24$ mm, $b = 30$ mm, $2w^{(i)} = 3.8$ mm, and $L = 6$, which will be called the second type. Before proceeding with numerical calculations, it is pertinent to check the convergence behavior of modal coefficients. Note that the modal orders to achieve sufficient convergence should be those of the propagating modes plus a few evanescent modes. Therefore, the truncation number of discrete modes for the azimuthal direction used in our computations is $N = 15$ ($n = 0, \pm 1, \pm 2, \ldots, \pm 15$) to achieve convergence to within 0.01%, which is used throughout numerical examples. Meanwhile, it is important to note that the aforementioned design parameters are determined by the design rules of rectangular grooves to have transmission through a slit maximized [24]. The previous study made it clear that the optimum conditions for the effective excitation of the spoof SPP modes are a period $p \approx \lambda$ and a depth $d \approx (2n + 1)\lambda/4$. The conditions were obtained using in-depth simulations, calculations, and experiments due to the difficulty in correlating the spoof SPP resonance frequency and a theoretical formulation. Therefore, we initially designed the first type and the second type according to the grooves' optimum
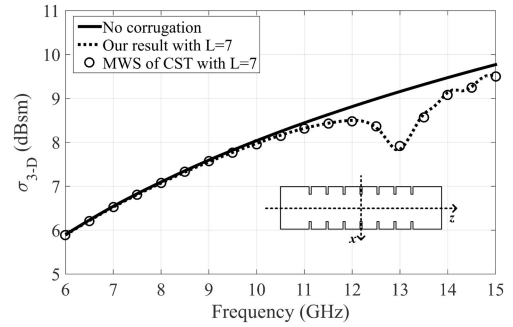

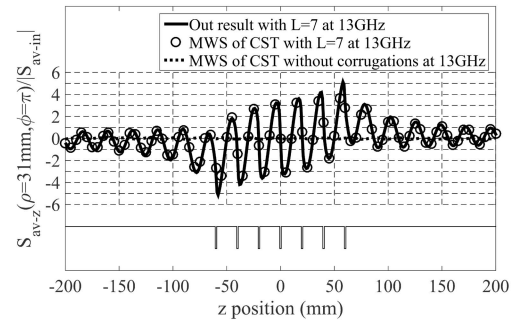Fig. 2. Monostatic RCS versus frequency ($\theta = 90°$, $\phi = 180°$).

Fig. 3. Ratio of the time-averaged Poynting vector toward z-direction near the conductor surface to the total magnitude of the time-averaged Poynting vector of the incident plane wave at 13 GHz.

conditions to figure out whether they can be applied to the circular cylinder with the corrugations.

Moving on to the validation of our theoretical formulation, we plotted monostatic RCS versus frequency at $\phi = 180°$ and $\theta = 90°$ in Fig. 2. The solid line denotes monostatic RCS of the smooth circular cylinder (no corrugations). The dotted line indicates our result of the first type, and circles stand for the simulation result of MWS of CST. As is well known, RCS of an infinite circular cylinder becomes nonfinite in general, and therefore, we assume that the total length of the circular cylinder is 1 m. This value will be used for all numerical examples unless otherwise specified. A comparison of our computational result to the simulation result shows a good agreement. The simulation was carried out based on the integral equation solver, 20 cells per wavelength, and a PEC as a material. The simulation time of MWS of CST is more than 30 min on a PC (Dual Intel Xeon CPU E5-2620 v3 at 2.40 GHz, 128 GB memory). For our formulation, the computation time is about 4 min on the same PC, implying that our formulation is more time-efficient to analyze electromagnetic behaviors of the proposed structure and to optimize the geometry. In fact, it is well known that surface waves can cause the reduction of reflection in both the optical and microwave regions. By converting a fraction of the energy of the incident wave into the surface energy, the reflected energy can be reduced in terms of the energy conservation. From Fig. 2, it is interesting to note that monostatic RCS is reduced the most at 13 GHz. Consequently, the excitation of the spoof SPP modes gives rise to the reduction of reflection in a certain direction (backscattering) and at a specific frequency.

To verify the existence of the surface waves, or the spoof SPP modes, Fig. 3 illustrates the ratio of the time-averaged Poynting vector toward z-direction $S_{\text{av-}z}(\rho, \phi, z)$ near the interface ($\rho = 31$ mm, $\phi = 180°$) to the total magnitude of the incident wave $|S_{\text{av-in}}|$.
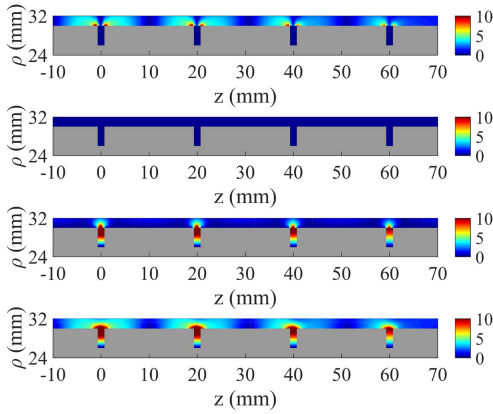
Fig. 4. Electric field amplitude in the case of the first type at 13 GHz ($\phi = 180°$). E_ρ, E_ϕ, E_z, and the total electric field from the top.

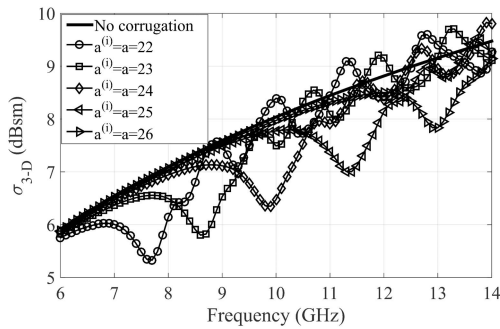Fig. 5. Monostatic RCS versus frequency as depth is varied in the case of the first type.

Fig. 6. Contour plot of monostatic RCS versus width and depth in the case of the first type at 13 GHz.

Fig. 7. Monostatic RCS versus frequency ($\theta = 90°$, $\phi = 180°$).

Circles denote the simulation result of MWS of CST and a comparison between the simulation result and our result shows a good agreement. Compared to the normalized time-averaged Poynting vector in the case of the circular cylinder without corrugations (see the dotted line), the normalized time-averaged Poynting vector of the first type is nonzero, even has a larger value. This demonstrates that the significant amount of energy flows along the corrugated surface. To further analyze the surface waves, we plotted the amplitude of E_ρ, E_ϕ, E_z, and the total electric field on the ρz-plane at $\phi = 180°$ in the case of the first type in Fig. 4. It is seen that the magnitude of the total electric field is intense both inside and outside the corrugations. It can be explained by the SPP theory. To be specific, the strong electric field within the corrugations results from cavity resonances, and the strong electric field above the corrugations is the spoof SPP modes coupled to the periodic corrugations [7]. The magnitude of E_ρ is much stronger near the corrugations' edge, which leads to increase in the Poynting vector toward z-direction. The intense field within the corrugations originates from mainly E_z; TM modes' resonance is dominant. The electric field distribution sufficiently supports the excitation of the spoof SPP modes. Therefore, we can say that the rectangular grooves' optimum conditions can be applied to the circular cylinder to sustain the spoof SPP modes.

It has been known that the spoof SPP modes can be generated on the surface of the circular cylinder with transverse corrugations [11]–[14]. However, it still seems to be lacking to study parameters including width, depth, and period for efficiently exciting the spoof SPP modes. Therefore, we conducted a parametric study to investigate a relationship between the spoof SPP resonance frequency and the parameters. First, the depth is varied, as shown in Fig. 5.
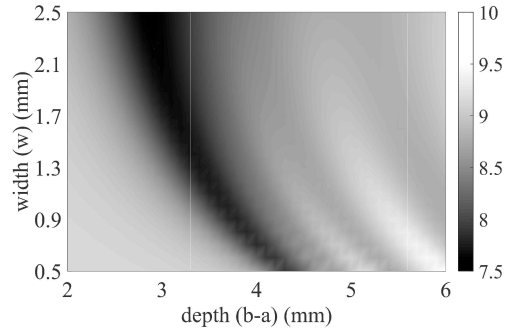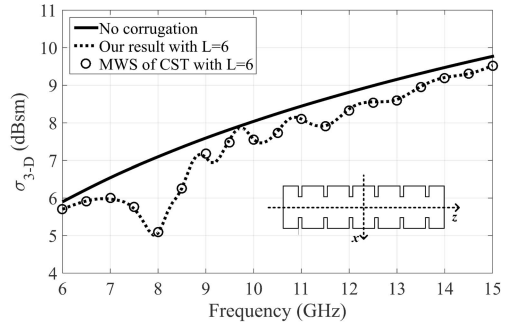
Note that the resonance frequency decreases as the depth increases, which coincides with the statement of the previous study [12]. In addition, Fig. 6 illustrates the contour plot of monostatic RCS versus the width and the depth. The width affects the resonance frequency as well, but its effect is minor. Once either the depth or the width is determined, it is feasible to optimize the other parameter with respect to monostatic RCS.

From now on, the increased period of the corrugations and the concomitant change in the resonance frequency will be investigated in detail by analyzing the second type. Fig. 7 illustrates monostatic RCS versus frequency at $\theta = 90°$ and $\phi = 180°$, and the resonance frequency is formed at 8 GHz, reducing reflection. Since the width is almost equivalent to $\lambda/10$ and the simulation result and the computed result are generally in good agreement, the assumption of a narrow corrugation is still valid. Therefore, we can conclude that the spoof SPP resonance frequency can be observed near the frequency corresponding to the period of the corrugations under the rectangular grooves' optimum conditions. We also plotted the ratio of the time-averaged Poynting vector toward z-direction $S_{\text{av-}z}(\rho,\phi,z)$ near the interface ($\rho = 31$ mm, $\phi = 180°$) to the total magnitude of the incident wave $|S_{\text{av-in}}|$ in Fig. 8 to illustrate the excitation of surface waves. Similar to the first type, considerable surface waves on the surface of the second type are generated. Fig. 9 shows the amplitude of E_ρ, E_ϕ, E_z, and the total electric field on the ρz-plane at $\phi = 180°$ in the case of the second type. The magnitude of E_ρ is mainly focused on the corner of the corrugations and the cavity resonance is due to E_z. We also plotted monostatic RCS versus frequency while varying the depth and the contour plot of monostatic RCS versus the width and the depth, as shown in Figs. 10 and 11, respectively. The resonance frequency is lowering as the depth increases, and the depth and the width can be optimized once one is determined. Therefore, appropriate values of the parameters make possible the excitation of the spoof SPP modes at a desired frequency.
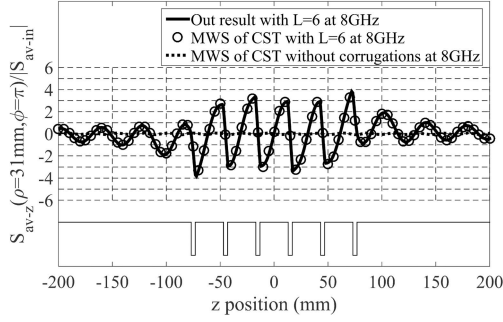
Fig. 8.   Ratio of the time-averaged Poynting vector toward z-direction near the conductor surface to the total magnitude of the time-averaged Poynting vector of the incident plane wave at 8 GHz.
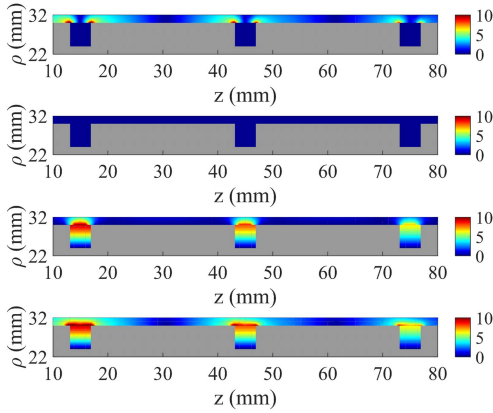

Fig. 9.   Electric field amplitude in the case of the second type at 8 GHz ($\phi = 180°$). E_ρ, E_ϕ, E_z, and the total electric field from the top.
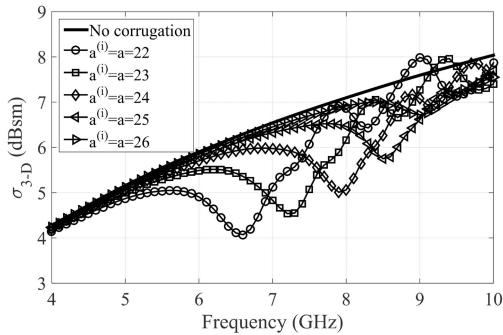

Fig. 10.   Monostatic RCS versus frequency as depth is varied in the case of the second type.

So far, scattering from two designed structures and the excitation of the spoof SPP modes have been investigated. The electric field distribution and the Poynting vector sufficiently demonstrate the existence of the spoof SPP modes. For the rectangular grooves in a planar conductor, a previous study revealed that the modulation of a depth can sustain the spoof SPP modes at multiple frequencies through in-depth simulations [21]. Thus, it is of significant interest to check whether one can excite the spoof SPP modes along the circular cylinder surface by modulating the transverse corrugations or not. Toward this purpose, we combined the first type and the second type into one structure and analyzed the structure in detail.
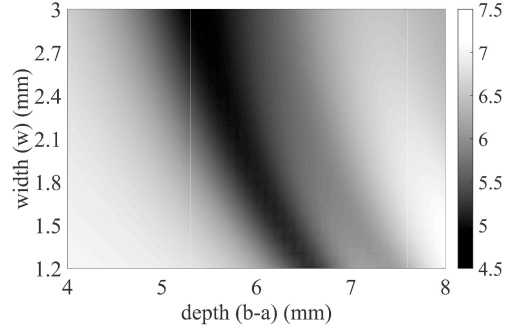

Fig. 11.   Contour plot of monostatic RCS versus width and depth in the case of the second type at 8 GHz.
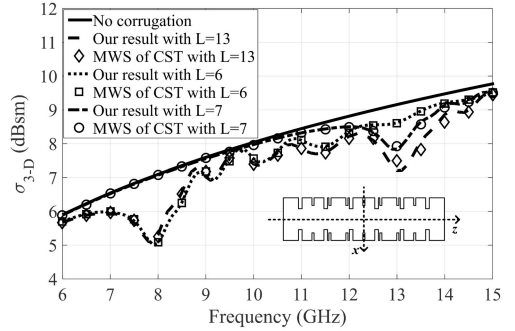

Fig. 12.   Monostatic RCS versus frequency ($\theta = 90°$, $\phi = 180°$).

To compare the performance of the first type, the second type, and the combined structure, we plotted monostatic RCS versus frequency in Fig. 12. The solid line indicates monostatic RCS of the circular cylinder without corrugations. The dashed line, the dotted line, and the dashed and dotted line denote monostatic RCS of the combined structure, the second type, and the first type, respectively. For all three structures, the simulation results and our results agree well. For the combined structure, it is seen that monostatic RCS is considerably decreased at both 8 and 13 GHz, compared to other frequencies. It is of interest that the combined structure shows two spoof SPP resonance frequencies of the first type and the second type with little to no deviation, whereas monostatic RCS value of the combined structure is almost equal to that of the second type at 8 GHz, discrepancy is observed at 13 GHz. As is shown in Figs. 5 and 10, above the spoof SPP resonance frequency, ripples appear, and this may be the reason for the discrepancy. As a result, it is feasible to sustain the spoof SPP modes at multiple frequencies by combining predesigned arrays of the corrugations.

V. CONCLUSION

The electromagnetic boundary-value problem of the modulated transverse corrugations in an infinite conducting circular cylinder is rigorously solved based on the Fourier transform, eigenfunction expansion, and the mode matching method. RCS was calculated in terms of the geometry of the corrugations and compared to the full-wave simulation results to validate our formulation. Due to the excitation of the spoof SPP modes, monostatic RCS can be reduced at a desired frequency. Also, modulating the corrugations leads to the excitation of the spoof SPP modes and the concomitant RCS reduction at multiple frequencies. Our theoretical formulation is useful to analyze and optimize the proposed structure and can be used in research on the reduction of reflection and the stealth technology as well.

REFERENCES

[1] C. Granet and G. L. James, "Design of corrugated horns: A primer," *IEEE Antennas Propag. Mag.*, vol. 47, no. 2, pp. 76–84, Apr. 2005.

[2] R. Levy, "Tapered corrugated waveguide low-pass filters," *IEEE Trans. Microw. Theory Techn.*, vol. MTT-21, no. 8, pp. 526–532, Aug. 1973.

[3] F. J. García-Vidal, H. J. Lezec, T. W. Ebbesen, and L. Martín-Moreno, "Multiple paths to enhance optical transmission through a single subwavelength slit," *Phy. Rev. Lett.*, vol. 90, no. 21, May 2003, Art. no. 213901.

[4] H. J. Lezec *et al.*, "Beaming light from a subwavelength aperture," *Science*, vol. 297, no. 5582, pp. 820–822, Aug. 2002.

[5] P.-S. Kildal, "Artificially soft and hard surfaces in electromagnetics," *IEEE Trans. Antennas Propag.*, vol. 38, no. 10, pp. 1537–1544, Oct. 1990.

[6] P.-S. Kildal, "Definition of artificially soft and hard surfaces for electromagnetic waves," *Electron. Lett.*, vol. 24, no. 3, pp. 168–170, Feb. 1988.

[7] F. J. García-Vidal and L. Martín-Moreno, "Transmission and focusing of light in one-dimensional periodically nanostructured metals," *Phys. Rev. B, Condens. Matter*, vol. 66, Oct. 2002, Art. no. 155412.

[8] F. J. García-Vidal, L. Martín-Moreno, and J. B. Pendry, "Surfaces with holes in them: New plasmonic metamaterials," *J. Opt. A, Pure Appl. Opt.*, vol. 7, no. 2, p. S97, Feb. 2005.

[9] D. Y. Na, J. H. Kim, Y. B. Park, and K.-Y. Jung, "Enhanced and directional transmission through a slit surrounded with grooves in a conducting plane," *IET Microw., Antennas Propag.*, vol. 7, no. 10, pp. 843–850, Jul. 2013.

[10] J. B. Pendry, L. Martín-Moreno, and F. J. Garcia-Vidal, "Mimicking surface plasmons with structured surfaces," *Science*, vol. 305, pp. 847–848, Aug. 2004.

[11] S. A. Maier, S. R. Andrews, L. Martín-Moreno, and F. J. García-Vidal, "Terahertz surface plasmon-polariton propagation and focusing on periodically corrugated metal wires," *Phy. Rev. Lett.*, vol. 97, no. 17, Oct. 2006, Art. no. 176805.

[12] A. I. Fernandez-Dominguez, L. Martin-Moreno, F. J. Garcia-Vidal, S. R. Andrews, and S. A. Maier, "Spoof surface plasmon polariton modes propagating along periodically corrugated wires," *IEEE J. Sel. Topics Quantum Electron.*, vol. 14, no. 6, pp. 1515–1521, Nov./Dec. 2008.

[13] H. Yao and S. Zhong, "Plasmonic corrugated cylinder-cone terahertz probe," *J. Opt. Soc. Amer. A, Opt. Image Sci.*, vol. 31, no. 8, pp. 1856–1860, Aug. 2014.

[14] Y. Chen *et al.*, "Effective surface plasmon polaritons on the metal wire with arrays of subwavelength grooves," *Opt. Express*, vol. 14, no. 26, pp. 13021–13029, 2006.

[15] G. Manara, A. Monorchio, G. Pelosi, and R. Coccioli, "Electromagnetic scattering from corrugated cylinders," in *IEEE Antennas Propag. Soc. Int. Symp. Dig.*, vol. 1, Jun. 1995, pp. 14–17.

[16] G. Manara, G. Pelosi, A. Monorchio, and R. Coccioli, "Plane-wave scattering from cylinders with transverse corrugations," *Electron. Lett.*, vol. 31, no. 6, pp. 437–438, Mar. 1995.

[17] T. C. Rao, "Plane wave scattering by a corrugated conducting cylinder at oblique incidence," *IEEE Trans. Antennas Propag.*, vol. 36, no. 8, pp. 1184–1188, Aug. 1988.

[18] S. Garcia, J. Bagby, and I. Morazzani, "Plane-wave scattering of a periodic corrugated cylinder," in *IEEE MTT-S Int. Microw. Symp. Dig. Int. Microw. Symp. (IMS)*, Jun. 2017, pp. 466–469.

[19] J. K. Park and H. J. Eom, "Radiation from multiple circumferential slots on a conducting circular cylinder," *IEEE Trans. Antennas Propag.*, vol. 47, no. 2, pp. 287–292, Feb. 1999.

[20] D. H. Shin and H. J. Eom, "Radiation from narrow circumferential slots on a conducting circular cylinder," *IEEE Trans. Antennas Propag.*, vol. 53, no. 6, pp. 2081–2088, Jun. 2005.

[21] X. Gao, J. H. Shi, H. F. Ma, W. X. Jiang, and T. J. Cui, "Dual-band spoof surface plasmon polaritons based on composite-periodic gratings," *J. Phys. D, Appl. Phys.*, vol. 45, no. 50, Dec. 2012, Art. no. 505104.

[22] C. A. Balanis, *Advanced Engineering Electromagnetics*, 2nd ed. New York, NY, USA: Wiley, 2012, pp. 27–305.

[23] R. F. Harrington, *Time-Harmonic Electromagnetic Fields*, 2nd ed. New York, NY, USA: Wiley, 2001, pp. 242–250.

[24] M. Beruete, I. Campillo, J. S. Dolado, J. E. Rodriguez-Seco, E. Perea, and M. Sorolla, "Enhanced microwave transmission and beaming using a subwavelength slot in corrugated plate," *IEEE Antennas Wireless Propag. Lett.*, vol. 3, pp. 328–331, 2004.